

SnS₂/Si nanowire vertical heterostructure for high performance ultra-low power broadband photodetector with excellent detectivity

Cite as: J. Appl. Phys. **129**, 053105 (2021); <https://doi.org/10.1063/5.0032604>

Submitted: 09 October 2020 . Accepted: 06 January 2021 . Published Online: 03 February 2021

 Sourav Das,  Kalyan Jyoti Sarkar, Biswajit Pal, Hasmat Mondal, Sourabh Pal, Rabaya Basori, and Pallab Banerji



View Online



Export Citation



CrossMark

ARTICLES YOU MAY BE INTERESTED IN

[Intrinsic memristive mechanisms in 2D layered materials for high-performance memory](#)
Journal of Applied Physics **129**, 050902 (2021); <https://doi.org/10.1063/5.0035764>

[Realization of high detectivity mid-infrared photodiodes based on highly mismatched AlInSb on GaAs substrates](#)

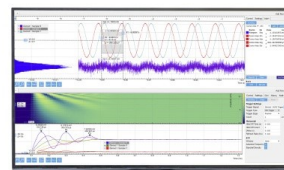
Journal of Applied Physics **129**, 053106 (2021); <https://doi.org/10.1063/5.0032563>

[Heterogeneously structured phase-change materials and memory](#)

Journal of Applied Physics **129**, 050903 (2021); <https://doi.org/10.1063/5.0031947>

Challenge us.

What are your needs for periodic signal detection?



Zurich
Instruments




SnS₂/Si nanowire vertical heterostructure for high performance ultra-low power broadband photodetector with excellent detectivity

Cite as: J. Appl. Phys. 129, 053105 (2021); doi: 10.1063/5.0032604

Submitted: 9 October 2020 · Accepted: 6 January 2021 ·

Published Online: 3 February 2021 · Publisher error corrected: 9 February 2021



Sourav Das,¹  Kalyan Jyoti Sarkar,^{2,a)}  Biswajit Pal,³ Hasmat Mondal,¹ Sourabh Pal,² Rabaya Basori,^{1,b)} 
and Pallab Banerji^{1,2,3}

AFFILIATIONS

¹School of Nano Science and Technology, Indian Institute of Technology Kharagpur, Kharagpur 721302, India

²Advance Technology Development Centre, Indian Institute of Technology Kharagpur, Kharagpur 721302, India

³Materials Science Centre, Indian Institute of Technology Kharagpur, Kharagpur 721302, India

^{a)}Current address: Department of Electronic Systems Engineering, Indian Institute of Science, Bangalore 560012, India.

^{b)}Author to whom correspondence should be addressed: rabaya@iitkgp.ac.in

ABSTRACT

Nanoparticle–nanowire heterostructures provide a new platform for photodetection applications owing to their higher light absorption, large responsivity, and excellent separation efficiency of photogenerated electron–hole pairs. Herein, we report a SnS₂/Si nanowire heterostructure photodetector with excellent optoelectronic properties. A high-quality SnS₂/Si nanowire heterostructure was prepared by simply spin coating a wet chemically synthesized SnS₂ on a vertically standing Si nanowire made by metal assisted chemical etching. The as-prepared SnS₂/Si nanowire heterostructure exhibits a robust p–n junction with excellent photodetector characteristics. The photodetector based on the heterostructure shows a photo-responsivity of $\sim 3.8 \text{ A W}^{-1}$, a specific detectivity up to $\sim 2 \times 10^{14}$ Jones, and an on/off ratio up to $\sim 10^2$ at 340 nm illumination wavelength with a significantly low optical power density of 53.75 nW/mm^2 at zero bias (0 V). The photo-responsivity reached its maximum value of $\sim 10^2 \text{ A/W}$ and detectivity of $\sim 1 \times 10^{14}$ Jones at the same wavelength with an applied bias of -2 V . In addition, the heterostructure photodetector provides significantly good photodetector key parameters (responsivity $\sim 5.3 \text{ A/W}$, detectivity $\sim 7.5 \times 10^{12}$ Jones, rise/decay time $\sim 0.4/0.4 \text{ s}$) at -2 V bias over a wide spectral range from 400 to 1100 nm. The Si nanowire and SnS₂ nanoparticle heterostructure devices with an enhanced junction area open up an exciting field for novel non-toxic and environmental friendly broadband optical detection applications and optoelectronic memory devices with high responsivity, ultrahigh sensitivity, and self-sufficient functionality at low power consumption and low cost with ease of processing.

Published under license by AIP Publishing. <https://doi.org/10.1063/5.0032604>

I. INTRODUCTION

Broadband photodetectors (PDs) from the ultraviolet (UV) to infrared (IR) region are key devices in current research and have a wide range of technological applications, including imaging, remote sensing, optical communication, analytics, and military surveillance.^{1–4} The most challenging issue pertaining to broadband PDs is the selection of materials with broad light absorption capability, high responsivity, superior detectivity, low noise, and high stability. However, even in recent times, separate sensors or materials have been required for different subbands (UV–visible to IR) to achieve the best operating performance. For example, GaN based

detectors work best in the UV region (0.25–0.4 μm), while Si- and InGaAs-based detectors are applied to visible (0.45 to 0.8 μm) and IR regions (0.9–1.7 μm), respectively.^{5–7} The detectivity of silicon photodetectors is $\sim 4 \times 10^{12}$ Jones and that of InGaAs photodetectors is $\sim 10^{12}$ Jones at room temperature, which limit their practical applications. To investigate high-performance photodetectors to be used at room temperatures, a variety of low dimensional photodetectors have been fabricated using graphene, WS₂, MoS₂, MoSe₂, SnO₂, ZnO, etc. in their pure form or as heterostructure composites.⁸ In recent times, although there are some reports on broadband photodetectors like InAs, In₂Se₃, and InP nanowires, it is still

a challenge to develop low-cost, nontoxic, high performance, and highly sensitive broad-response photodetectors that could be used at room temperatures.^{9–11}

Chalcogenides have many extraordinary characteristics and considerable potential in various applications like light-emitting devices, lithium-ion batteries, and solar cells.^{12–14} The crystal structures of the chalcogenides are mainly exhibited as metal atoms like Mo, W, Ga, and Sn, sandwiched between three chalcogen layers such as S, Se, and Te, forming the general formula YX_2 . Tin disulfide (SnS_2) belongs to an important member of the chalcogenide family in which the tin (Sn) atoms are located between two sulfur (S) slabs to form a three-atom sandwich structure that usually has a hexagonal crystal structure. In addition, it is noteworthy that SnS_2 has a tunable bandgap and exhibits a remarkably high photoresponse.¹⁵ Besides, owing to its appropriate optical and electronic properties, SnS_2 is low cost and nontoxic, and its component elements are readily available, which makes it promising for optoelectronic applications.¹⁶ Recently, there have been some reports on SnS_2 based photodetectors that manifest notable application potentials.¹⁷ However, as the photocurrent of these photodetectors is low and they have dark current, they have poor detectivity. As a result, the reported SnS_2 based photodetector becomes inappropriate for actual device application. At present, it remains a big challenge to produce optical detectors that can be operated with a larger responsivity and ultra-high detectivity over a wide range of wavelengths. Furthermore, from the results reported earlier, it is also confirmed that only SnS_2 cannot simultaneously satisfy efficient light absorption and suitable band alignment that can govern the photoexcited carriers to fulfill all the above criteria. In addition, bandgap misalignment near the interface may also result in poor performance of detectors. Therefore, many attempts still need to be made to improve the device performance of SnS_2 by making heterostructures with suitable materials. A recent report by Xu *et al.* shows that SnS_2 has a good light absorption and suitable band alignment with bulk Si.¹⁸ However, dark current is quite high, which suppresses the optoelectronic performance or efficiency of the reported device. Therefore, for achieving high-performance nanoscale optoelectronic devices, it is of utmost importance to ascertain new processing methods and to optimize device structures. Furthermore, the built-in-potential created at the interface of the heterojunction performs a significant role in the highly efficient separation of photogenerated electron-hole carriers participating in the photocurrent.¹⁹ Thus, enhancing the interface is one way to improve the optoelectronic performance of a device, and materials in the form of nanowires are the best choice due to their large surface-to-volume ratio.

Silicon nanowires (SiNWs) are widely used photoresponsive materials satisfying most of the requirements for technological applications. SiNWs are of particular interest due to their low cost, easy synthesis process, and the ability to integrate with conventional fabrication techniques. In addition, Si in nano becomes a direct bandgap material that overcomes the problem of poor optical absorption in bulk material.²⁰ SnS_2 has a good light absorption and suitable band alignment with Si.¹⁸ However, optical detection devices based on the heterostructure of SnS_2 with other optoelectronic materials have received far less attention than other devices, and photodetectors based on the SnS_2 NP/SiNW heterostructure have not been realized yet, although such a heterostructure has excellent broadband light absorption, suitable band alignment, and high optical performance

with ultra-high detectivity. Therefore, the integration of SnS_2 NPs with the advanced SiNW technology becomes very important and meaningful for practical optoelectronic device applications particularly in noisy environments. So far, the device physics based on the SnS_2 /SiNW heterostructure has not been well explored, and, therefore, device optimization remains to be fully revealed.

In this article, we have reported a heterostructure of SnS_2 NPs with a vertically aligned SiNW to improve the optical performance in the ultraviolet (UV) to near-infrared (NIR) regions (300–1100 nm). The fabricated heterostructure shows an optical bandgap (E_g) of p-SiNW ~ 1.43 eV (direct) and n- SnS_2 with $E_g \sim 2.83$ eV (direct). The photoelectric conversion behavior was studied under illumination from UV to NIR sources. The SnS_2 /Si NWs heterostructure device exhibited a remarkably high photoresponsivity, ultra-high detectivity with very low illumination power, and wide wavelength range of operation compared with other similar devices. These results are analyzed using a band diagram with an estimated built-in potential and depletion region near the interfaces, depending on the heterostructure determining the dynamics of the charge carrier.

II. EXPERIMENTAL SECTION

A. Material synthesis and device fabrication

Arrays of vertical SiNWs were fabricated from a commercial Si wafer [p-type, (100)-oriented, $0.01 \Omega \text{ cm}$ resistivity] by the metal assisted chemical etching (MACE) method.^{21,22} MACE is preferred for NW synthesis as it offers the advantages of cost-effectiveness, simplicity, large scale, and wide availability to researchers. Other synthesis processes like reactive ion etching (RIE) require access to clean room facilities, and vapor-liquid-solid (VLS) synthesis generates impurities that can alter an NW's electronic properties due to the use of a metal catalyst.²³ Nanowires produced via MACE have the pristine composition and crystalline orientation of the parent of p-Si wafer. In the MACE process, a cleaned Si wafer was immersed in a silver (Ag) coating solution containing 4.8M HF and 0.01M AgNO_3 for 30–50 s, resulting in a uniform Ag nanoparticle layer deposited on the Si wafer. Highly dense nanowires were formed after immersing Ag coated Si wafer in an etchant solution containing HF (40%), H_2O_2 (30%), and DI water with a volume ratio of 1:1:3 for 1 h. Ag nanoparticles coated on the Si substrate help the underneath silicon to react with HF in the presence of H_2O_2 . This process proceeds downward with time, leading to the formation of vertically standing SiNW arrays. Finally, residual Ag nanoparticles were removed by putting Si NW arrays into a dilute aqua regia ($\text{HNO}_3:\text{HCl}:\text{H}_2\text{O} = 1:3:2$) solution. The growth mechanism is elaborated in the [supplementary material](#).

The SnS_2 nanoparticles (NPs) used in this study were synthesized by the wet chemical method.²⁴ Initially, a solution was prepared in a beaker by dissolving 0.8 g of tin(IV) chloride pentahydrate ($\text{SnCl}_4 \cdot 5\text{H}_2\text{O}$) in 2 ml conc. HCl (35% w/w) and stirred for 5 min. Then, 30 ml of DI water and 0.25 g of thioacetamide were added one by one to the solution under constant stirring. The stirring was continued for 3 h until the solution turned into yellow color. After that, 18 ml of DI water was added to make the final solution of 50 ml. The final solution was kept in isolation for 25–30 min to settle down the yellow particles at the bottom. The product was filtered and washed with DI water followed by

methanol several times to obtain SnS₂ nanoparticles. After several washes, the precipitates were dried in an oven at 45 °C for 5 h. The SnS₂ NPs showed an n-type electrical conductivity.^{25,26} The as-synthesized SnS₂ NPs were then used for further study.

The heterostructure of the SnS₂/p-Si NWs was fabricated by spin coating of the SnS₂ NPs suspended in 2-propanol solution on Si NWs at 1000 rpm followed by drying at 80 °C for 10 min and finally annealed at 120 °C for 1 h in nitrogen atmosphere. Just before spin coating, the Si NWs wafer was cleaned with HF to remove the native oxide layer from the NW surface. The scanning electron microscopy (SEM) image of the fabricated heterostructure is shown in Fig. 1(a), where Fig. 1(b) shows Si NWs of diameter ~90–100 nm before SnS₂ NP dispersion, and Fig. 1(c) of the same shows the vertically aligned SiNWs decorated with SnS₂ NPs. After SnS₂ coating on the surface and top of Si NW, the top Au (40 nm) contacts were then deposited by electron beam evaporation of the Au metal onto SnS₂ NPs on top of SiNWs. The bottom Al contact was deposited by thermal evaporation on the back of the Si wafer. The top contact area of the heterostructure was calculated to be 0.2 mm². The device fabrication process is described stepwise schematically in Fig. S2 in the [supplementary material](#).

B. Structural and morphological characterization

The morphology and the crystallinity of SnS₂ were characterized and analyzed by x-ray diffraction (XRD) using a Rigaku MiniFlex600

diffractometer with Cu K α radiation (wavelength 1.54 Å), scanning electron microscope (SEM) (Marlin), energy dispersive x-ray spectroscopy (EDAX) attached to an SEM and transmission electron microscope (TEM) (JEOL, JEM-2100F, 200 kV) with a selective area electron diffraction (SAED) pattern, and Raman spectroscopy was done by using an excitation Argon-Krypton mixed ion gas laser (Coherent Innova 70C) attached with MODEL 2018 RM (Make Spectra Physics, USA) attached with Spectrometer MODEL T64000 (Make Jobin Yvon Horiba, France), Detector Thermoelectric cooled front illuminated 1025 × 256 CCD, MODEL Syncerity (Make Jobin Yvon Horiba, France).

C. Device performance characterization

The optical absorption was measured by using a UV–Vis–NIR spectrophotometer (Hitachi UH4150). The room temperature PL measurement was done using a Horiba Fluoromax 4CP spectrofluorometer at a 450 nm excitation wavelength. The *I*–*V* characteristics, spectral response, and optoelectronic measurements of the SnS₂/SiNW heterostructure were evaluated at room temperature using a semiconductor parameter analyzer (4200-SCS, Keithley) and a Newport IPCE measurement system with a broadband light source and a monochromator. The intensity of the illuminated light was measured using an optical power meter (ThorLabs, PM400).

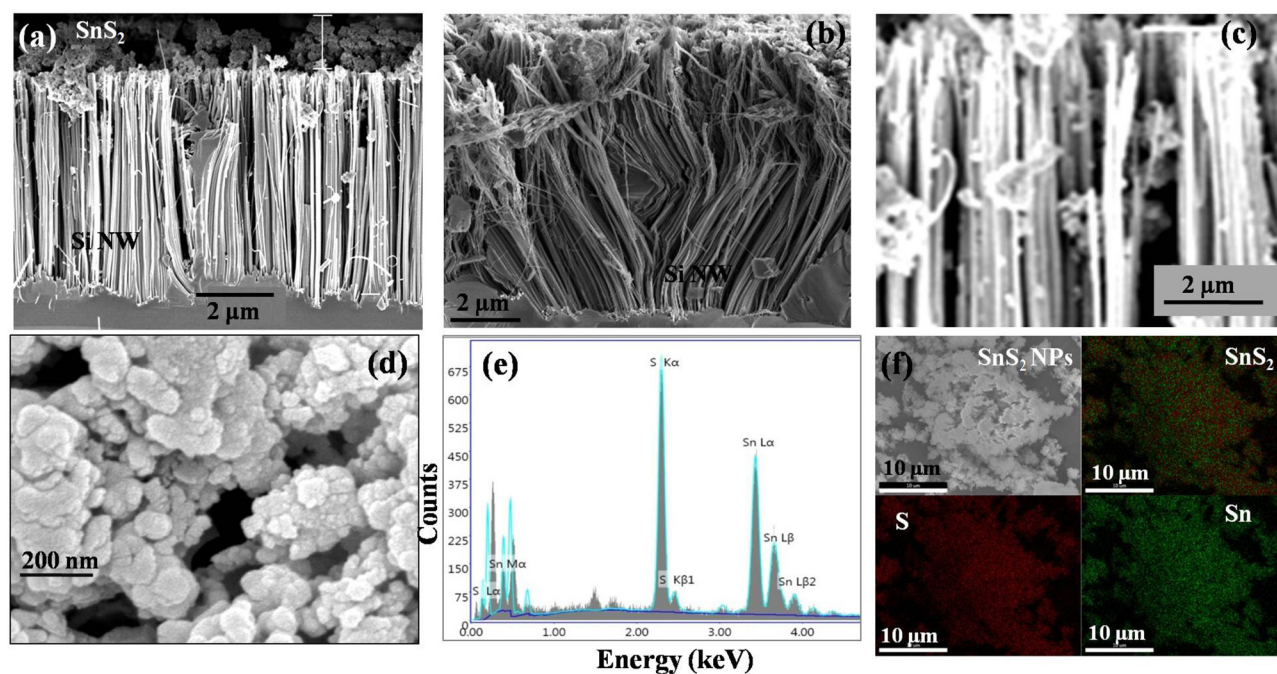


FIG. 1. (a) Cross-sectional FE-SEM images of the SnS₂/SiNW heterostructure. Si NWs (b) without and (c) with SnS₂ NP decoration showing SnS₂ NPs on the surface of Si NWs. (d) Top view of aggregated SnS₂ NPs on top of a SiNW array. (e) EDX spectrum and (f) chemical elemental mapping of SnS₂ NPs which confirm the uniform distribution of S and Sn atoms throughout the entire aggregates of SnS₂ NPs.

III. RESULTS AND DISCUSSIONS

A. Structural and morphological analysis

1. SEM analysis

The cross-sectional SEM image of the SnS₂/SiNW heterostructure shown in Figs. 1(a) and 1(b) shows the MACE grown Si NWs. The length of the NW array was $\sim 10\ \mu\text{m}$ for a growth time of ~ 30 min and the thickness of the SnS₂ NPs on top of the NW array was ~ 100 nm. The diameter of the Si NWs ranged from 90 to 100 nm and that of SnS₂ NPs was ~ 8 to 10 nm. The SEM image of the SnS₂ NPs coated on top of the Si NW array is shown in Fig. 1(d). The EDAX analysis images are shown in Figs. 1(e) and 1(f) where edax spectra and chemical compositional mapping, respectively, are also shown. The Sn and S elements are uniformly distributed throughout the entire aggregate of the SnS₂ NPs.

2. XRD analysis

The crystal phase of the SnS₂ NP powder was investigated by x-ray diffraction (XRD) and its corresponding pattern scanned in the range of $2\theta = 10^\circ$ – 90° is presented in Fig. 2(a). The peaks observed for the SnS₂ NPs are consistent with the peaks of SnS₂ thin films as reported earlier.^{27,28} The diffraction peaks of the SnS₂ NPs observed at 14.98° , 26.18° , 28.79° , 33.54° , 50.76° , 60.69° , and

62.20° correspond to the (001), (100), (002), (101), (110), (201), and (004) crystal planes (JCPDF 89-2028). No unknown peaks were seen, which confirms the purity of the materials. TEM analysis was further carried out to analyze the structure of the sample.

3. TEM analysis

To obtain in-depth information on the SnS₂ NP shape and crystallinity, high-resolution TEM (HRTEM) with SAED pattern was also performed. The TEM image of the SnS₂ NPs is shown in Fig. 2(b). The average size of the SnS₂ NPs is ~ 8 – 10 nm, as shown in Fig. 2(c), and the same result has been obtained from SEM also [Fig. 1(b)]. The SAED pattern taken from one of the dispersed NPs is depicted in Fig. 2(d). It manifests the polycrystalline nature of the SnS₂ NPs. The corresponding planes for the zone axis $[-110]$ are (002), (110), (004), (211), and (220) and from XRD in Fig. 2(a) we can confirm the presence of these planes. Figure 2(e) reveals the HRTEM image of one such NP with a d-spacing of ~ 0.342 Å and corresponds well with SnS₂ (201).²⁹

4. Raman analysis

Another approach followed to identify the crystal quality of the SnS₂ NPs was Raman spectroscopy. The micro-Raman spectra are presented in Fig. 2(f). The presence of the A_{1g} optical phonon

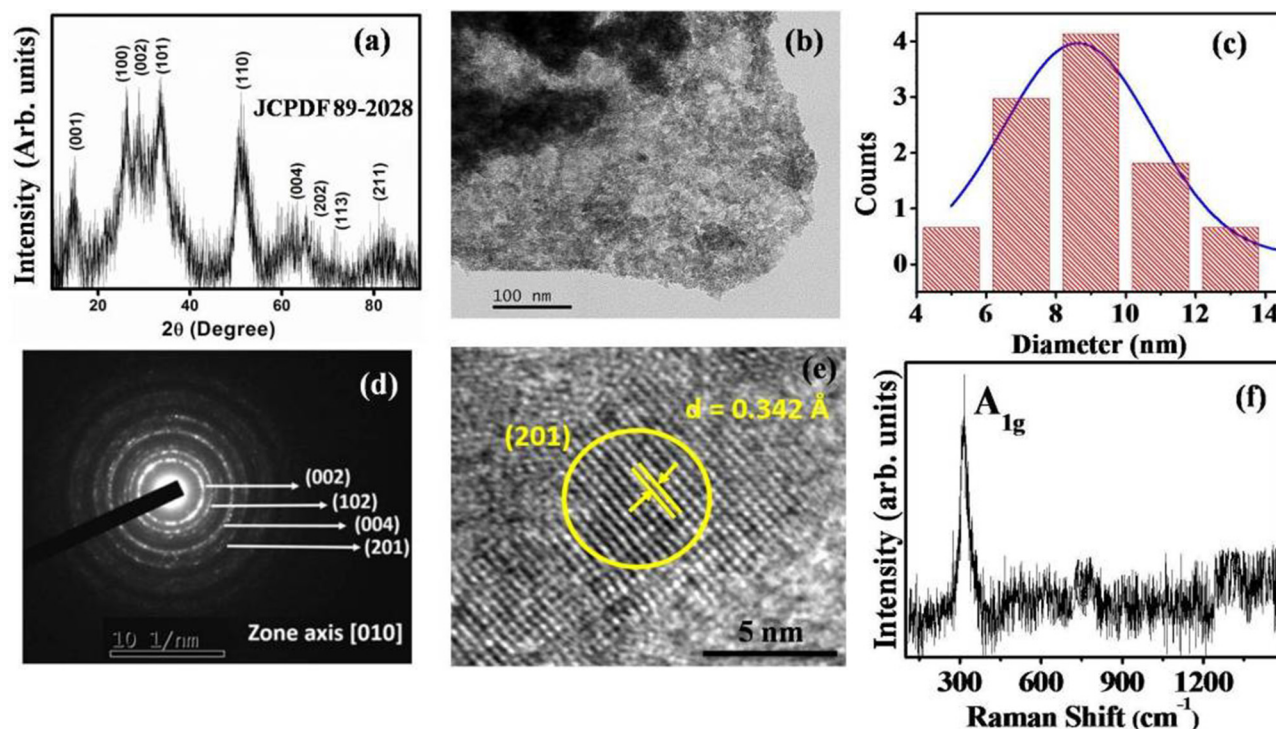


FIG. 2. (a) XRD patterns of SnS₂ NP powder. (b) TEM image of SnS₂ NPs with (c) a particle size distribution curve and (d) SAED pattern showing different crystal planes. (e) HRTEM image showing d-spacing of SnS₂ NPs taken from the top portion of (b). (f) Raman spectra of SnS₂ NPs. The presence of the A_{1g} optical phonon mode confirms the formation of SnS₂.

mode at $\sim 313.5 \text{ cm}^{-1}$ confirms the formation of SnS_2 ,^{16,30} although the E_g phonon mode, which is generally present in bulk SnS_2 , is absent here due to the presence of nanostructures.¹⁶

B. Optical analysis

1. Absorption

Figure 3(a) shows the UV-visible spectra of SiNWs (blue curve), SnS_2 NPs (red curve), and the SnS_2/SiNW mixture in methanol (green curve), respectively. Significant enhancement in absorption is observed in the hybrid structure compared with the individual one mostly in the UV range. For the SnS_2 NPs, a strong absorption was observed in the UV region. However, in the case of the SiNWs, a broad absorption was observed with an almost constant intensity. The combined effect of SnS_2 and SiNWs showed an improved absorption. The bandgap (E_g) of the material was calculated using the equation $(\alpha h\nu)^2 = B(h\nu - E_g)$, where α , $h\nu$, and B are the absorption co-efficient, photon energy, and constant of the material, respectively.³¹ The optical bandgap was extracted from the Tauc plot of $(\alpha h\nu)^2$ vs $h\nu$ that yielded 0.17 cm^{-1} and 0.18 cm^{-1} absorption coefficients and 1.45 eV and 2.83 eV bandgap for the Si NW array and SnS_2 NPs, as shown in Fig. 3(b). This is in good agreement with the values achieved for the SiNWs of different diameters through various MACE methods.^{32,33} The bandgap of SnS_2 is also consistent with the other reported works irrespective of the synthesis methods.^{15,16,28} The improved absorption in the hybrid structure signifies the enhanced optoelectronic properties that will be useful for future optoelectronic applications.

2. Photoluminescence

The room temperature PL emission spectra for the SnS_2 NPs and SiNWs were measured at a 300 nm excitation wavelength to

investigate whether there were any defects, vacancies, and gaps inside the material, and are shown in Fig. 4. The SnS_2 nanoparticles mainly have four peaks, as shown in Fig. 4(a). Notably, the most intense peak is at 437 nm, which originates due to the exciton recombination corresponding to the near band emission of the SnS_2 wide bandgap caused by the quantum confinement effects.³⁴ Meanwhile, the blue light at the center of 485 nm can be attributed to the self-activation center formed by the tin vacancies in the lattice or the energy transfer between the sulfur vacancies and the sulfur gap. The yellow light at 581 nm and the red one at 850 nm are mainly defect-related luminescence-like surface defects, interstitial sulfur vacancies, and SnS_2 lattice gap defect of shallow deep and deep traps.³⁵ The PL spectra of the SiNWs in Fig. 4(b) consist of a broad band in the visible range with the maximum peak intensity at around 650 nm. This broad peak is observed due to the radiative recombination of excitons confined in small crystals created during nanowire growth by wet chemical etching.³⁶ When a hetero-junction is formed with Si NWs, emitted light from SnS_2 is reabsorbed by the SiNWs, contributing to further photo-carrier generation. From PL spectra of SnS_2 , we have calculated the energy bands corresponding to the peaks valued at 437 nm, 485 nm, 581 nm, and 850 nm. The most intense peak was found at 437 nm. The respective values corresponding to the peaks were 2.83 eV, 2.56 eV, 2.13 eV, and 1.45 eV. From these values, we can conclude that the energy band value that we have measured from the UV-vis graph, i.e., $E_g \sim 2.83 \text{ eV}$, is almost the same with the most intense peak's energy value of PL spectra.

C. Optoelectronic analysis

1. I-V characteristics

The schematic diagram of the device fabricated with a SnS_2/SiNW heterostructure and its corresponding mode of measurement

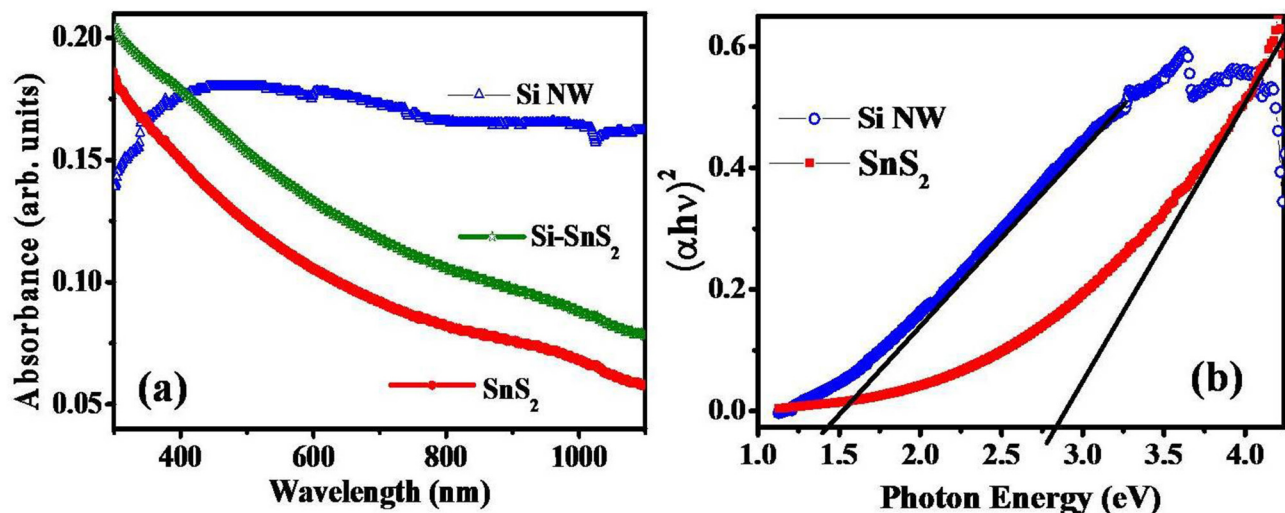


FIG. 3. (a) Optical absorption spectra of SiNWs (blue curve), SnS_2 NPs (red curve), and the SnS_2/SiNW hybrid structure (green curve), respectively, and (b) the corresponding Tauc plots confirming the optical bandgap $E_g \sim 1.4 \text{ eV}$ for SiNW and 2.85 eV for SnS_2 NPs.

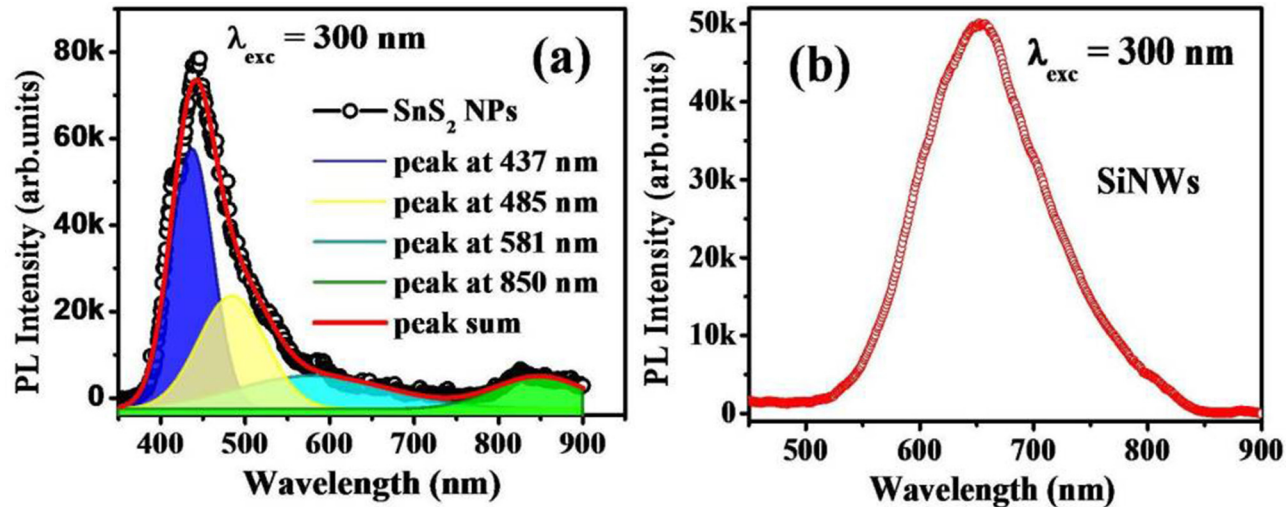


FIG. 4. Room-temperature PL spectrum of (a) SnS₂ nanoparticles and (b) Si nanowires at a 300 nm excitation wavelength.

is represented in Fig. 5(a), whereas Fig. 5(b) shows the photograph of the actual device. It has been reported that the top Au and bottom Al electrodes make very good ohmic contacts with SnS₂ and the Si layer, respectively.^{37,38} As illustrated in Fig. 5(a), the monochromatic incident light was produced by a commercial broadband light source attached to a monochromator. The active area of the photodetector is considered as the area of the SnS₂ NPs covered with an Au electrode of $\sim 0.20 \text{ mm}^2$ (spot diameter $\sim 0.5 \text{ mm}$). The illuminated spot on the sample is adjusted in such a way that it covers only the defined device area. Figure 5(c) represents the typical dark and light current–voltage (I – V) characteristic curves of the photodetector illuminated with different wavelengths ranging from 300 to 1100 nm in a semi-logarithmic scale. A minimum dark current of $\sim 1.6 \times 10^{-10} \text{ A}$ is obtained at zero bias. A maximum photocurrent of $\sim 4 \times 10^{-8} \text{ A}$ at the same bias is obtained under illumination with 340 nm light, which is close to the bandgap of SnS₂. Thus, an increment of current of $\sim 2.5 \times 10^2$ order is achieved at $V = 0 \text{ V}$ in this heterostructure device which opens up possibilities for a self-driven photodetector in future. This also reveals that the device has a much higher sensitivity to the incident 340 nm light. Furthermore, the I – V curve under light illumination shows that the photocurrent mainly forms at the applied reverse bias voltages, and it saturates with increasing bias. The different behavior of photocurrents at positive and negative bias voltages indicates that the photodetectors based on the photovoltaic effect have been prepared successfully.

To understand the photo-carrier transport mechanism, i.e., electron–hole pair generation and separation, we proposed a band diagram. Based on the extracted bandgap energy from the absorption curve, the band structure alignment of the SnS₂/SiNW heterostructure at thermal equilibrium is represented in Fig. 5(d). Generally, the electron affinities of SnS₂ and Si locate at 4.22 eV and 4.05 eV, respectively.¹⁷ The valence band values of SnS₂ (7.05 eV) and SiNW (5.47 eV) in the band diagram were calculated

by adding the bandgap energy as obtained from the absorption spectra to the electron affinity values. At thermal equilibrium, a depletion region is formed at the interface of n-type SnS₂ NPs and p-type SiNWs, resulting in the generation of a built-in field at the interface directed from n-SnS₂ to p-SiNWs. When light with photon energy larger than the bandgap is incident on the device surface, the energy from the incident photons will be absorbed by the SnS₂ NPs as well as by the Si NWs. The valence electrons in SnS₂ will be excited and will jump into the empty conduction band. As a result, the high-density electron–hole pairs will be generated in the SnS₂ NPs during illumination, as displayed in Fig. 5(e). These will be added up with the large number of electron–hole pairs generated in the depletion layer created at the interface. The photogenerated electron–hole pairs at the depletion region will be separated by the built-in field which effectively drives the holes toward p-SiNW and electrons toward n-SnS₂, as shown in Fig. 5(e). The photogenerated holes in the valence band of n-SnS₂ will be driven into the p-SiNW side by the built-in field, while those photogenerated electrons in the conduction band will move in the opposite direction. These will result in an increase of potential in p-SiNW, while there will be a reduction of the same in the n-SnS₂ side. Thus, a photo-induced voltage will be generated across the junction that effectively reduces the barrier height of the SnS₂/SiNW heterostructure, and a detectable photocurrent is obtained in the external circuit. When reverse bias is applied externally in the circuit, an additional potential (V_b) will be introduced along with the photo-induced voltage, as shown in Fig. 5(f), and accelerate the photocarrier transport by reducing the transit time and recombination rate. As a result, the photocurrent increases with increasing the bias voltage. When a forward bias is applied across the junction, the external potential (V_b) will be in the opposite direction of the photo-induced voltage and the effective potential across the junction will be reduced, as shown in Fig. 5(g). This will effectively reduce the photocarrier transport by increasing

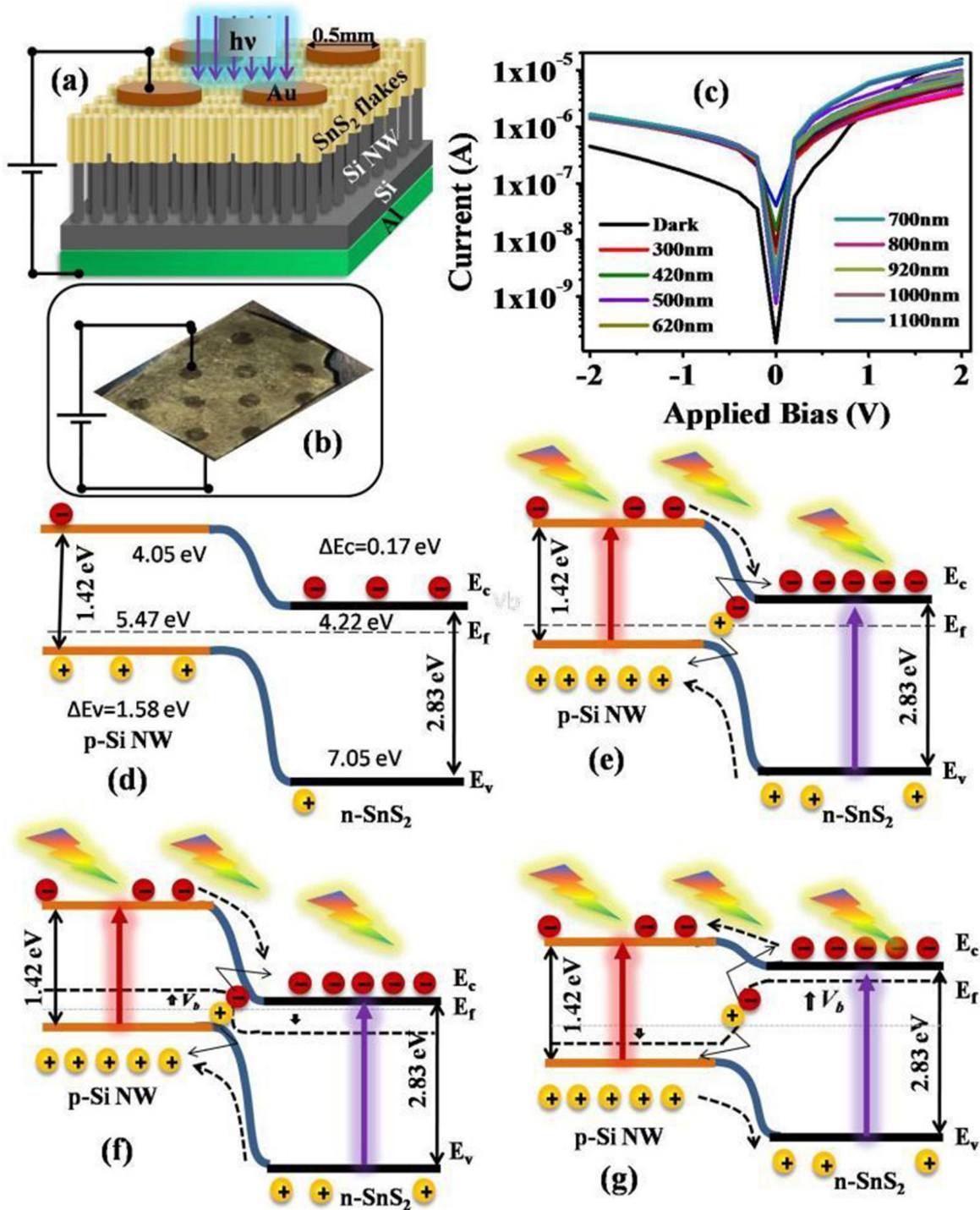


FIG. 5. Photoelectric transport investigations of SnS₂/SiNW heterojunctions. (a) Schematic representation of the heterostructure device under test. (b) Actual photograph of the device under test. (c) I-V characteristics of the SnS₂/SiNW heterostructure device in the dark and under illumination with different wavelengths. (d) Energy-band alignment between the SnS₂ NP and SiNWs junction at thermal equilibrium. (e) Self-driven mechanism of the detector at 0 V under light illumination. (f) Energy-band alignment with an applied external reverse bias voltage (V_b). (g) Energy-band alignment with an applied external forward bias voltage (V_b).

the transit time and recombination rate compared with that of the reverse bias. Thus, the enhancement of photocurrent in the forward bias is negligible, as observed in Fig. 5(c). In this heterostructure, the built-in field created at the interface is high enough to separate and transit the photo-generated carriers to the electrodes and give a sufficiently high photocurrent, even if no bias is applied externally.

2. Spectral response

Figure 6 represents the spectral response of the heterostructure photodetector device for different parameters. Figure 6(a) represents photocurrent over dark current at zero bias as a function of wavelength, and the photo-to-dark current ratio exceeds 10^2 at $V=0$ V, which is considerably high for this type of heterostructure.^{27,39} As seen from Fig. 6(a), the heterostructure exhibits a high photo-sensitivity ($I_{\text{illu}} - I_{\text{dark}}/I_{\text{dark}}$) exceeding 10^2 at $V=0$ V over a wide range of wavelength, and confirms its ability of better noise rejection, where the photocurrent is clearly distinct from the dark current. The photo responsivity (\mathcal{R}) can reflect the sensitivity of a heterojunction photodetector to the incident light, and thus it gradually becomes the significant figure of merit for light detection devices. The responsivity was calculated from 300 to 1100 nm under a differently applied bias using the equation $\mathcal{R} = I_{\text{ph}}/P_{\text{sample}}$ as reported earlier.⁴⁰ Here, $I_{\text{ph}} = (I_{\text{illu}} - I_{\text{dark}})$ and $P_{\text{sample}} = P \times A$, where P is the illuminated power density and A is the effective device area under illumination. Therefore, based on this formula, the responsivity (\mathcal{R}) of the SnS₂/SiNW detector at a different bias as a function of wavelength was estimated, and it is depicted in Fig. 6(b) in a semi-logarithmic scale. As seen from the figure, the responsivity in the UV region is as high as ~ 3.8 A/W with the self-bias (0 V) condition; it reaches $\sim 10^2$ A/W at an applied bias of -2 V and it reduces in the visible to NIR region. Notably, a sharp peak appears at 340 nm. The responsivity (\mathcal{R}) of the device shows a monotonically increased tendency with increasing the applied bias voltage and approaching toward saturation, as illustrated in Fig. 6(c). With increasing bias, the transport and the separation of the photogenerated electron-hole pairs first accelerate and then enhance the photoresponsivity (\mathcal{R}) of the device. At a higher bias voltage, all photogenerated electron-hole pairs are collected by the electrodes before recombination and a further increase of bias voltage has a negligible effect on the photocurrent, resulting in a saturation of \mathcal{R} , as shown in Fig. 6(c). It is also observed that the responsivity is very high ($\sim 10^2$ A/W at -2 V) at ~ 340 nm with a gradual reduction at other wavelengths. Most importantly, the responsivity is at least ~ 3.5 A/W at -2 V over the wide range of wavelength (300–1100 nm) and exceeds the responsivity values of photoconductive photodetectors reported recently.^{17,19,25} In the self-driven mode, the responsivity is as high as ~ 3.5 mA/W over a wide spectral range (300–1100 nm) and reaches 3.8 A/W at 340 nm (light intensity 53.75 nW/mm²). The peak high responsivity at ~ 340 nm is close to the bandgap of the SnS₂ NPs. The spectral response is also correlated with the main PL emission at ~ 340 nm in Fig. 5, as discussed earlier. The overall high responsivity (~ 3.8 A/W) over the wide range of wavelength is attributed to the combined effect of the photoresponsive property of the junction materials and the increased light absorption capability of the

heterojunction due to the nanostructure forms of both SnS₂ and Si. Such high responsivity of the heterostructure over the wide spectral range with a significantly small optical power (optical power density \sim nW/mm² range) shows that it is superior to the other reported devices based on SnS₂.^{17,22,41–43} and indicates its possibility to be used as a broadband photodetector. In addition, another important parameter for a heterojunction detector is detectivity (D^*), which is the inverse of noise equivalent power. The larger the detectivity of a photodetector, the more it is suitable for detecting weak signals that compete with the detector noise. Therefore, we can calculate the detailed values of the detectivity (D^*) by using the equation $D^* = A^{1/2} \mathcal{R} / (2qI_{\text{dark}})^{1/2}$, where I_{dark} is the dark current, A is the effective device area under illumination, and q is the electronic charge.^{15,44} Based on this formula, we estimated the detectivity (D^*) of the photodetector as a function of illumination wavelength, and the calculated detectivity (D^*) vs illumination wavelength curves at 0, -1.0 , and -2.0 V are plotted in Fig. 6(d) in a semi-logarithmic scale. Since the detectivity is dependent on dark current, and the dark current at the self-driven mode ($\sim 1.6 \times 10^{-10}$ A) is much lower than that at the bias dependent mode ($\sim 4.5 \times 10^{-7}$ A at -2 V), the heterostructure exhibited a higher detectivity (2.4×10^{14} Jones) at the self-driven mode at a wavelength of ~ 340 nm. This shows the highest detectivity ($\sim 2.4 \times 10^{14}$ Jones) among the SnS₂ based heterostructure reported to date, as shown in Fig. 6(e), which confirms its possibility as a high sensitivity photodetector at a particular wavelength of ~ 340 nm. In addition, the detectivity (D^*) is as high as $\sim 10^{12}$ Jones for 0 V over a wavelength of 300–1100 nm. More importantly, the external bias voltage can significantly improve the detectivity (D^*) of photodetectors, as shown in Fig. 6(d), and the almost constant $\sim 10^{13}$ Jones over a broad spectral range and far better than previously reported SnS₂ based heterostructures.^{22,24–26} Xu *et al.*¹⁸ reported a SnS₂/Si heterostructure showing a responsivity of ~ 0.12 A/W and detectivity of $\sim 9.35 \times 10^{10}$ Jones with an optical power density 0.5 mW/cm², whereas our reported heterostructure of the same materials with nanowire forms (SnS₂/SiNW) shows outstanding optoelectronic properties (a responsivity of >3.0 A/W with a peak value of $\sim 10^2$ A/W and detectivity of $>3.85 \times 10^{12}$ Jones with a peak value of $\sim 1.14 \times 10^{14}$ Jones), even with a much low optical power density (~ 0.54 nW/cm²) at the same working voltage. This enormous enhancement of optoelectronic performance is due to the enhanced interface area in nano. When two materials form a junction, the built-in-potential created at the interface of the heterojunction helps separate the photogenerated electron-hole pairs participating in the photocurrent. The surface area in the nanowire form is much higher than that in bulk Si due to the large surface-to-volume ratio in nano. Hence, the effective junction or interface area is enhanced enormously in the nanowire heterostructure compared with its bulk form, which effectively improves the performance of the heterostructure device for a highly efficient separation of photogenerated electron-hole carriers by creating a built-in-potential at the interface. Furthermore, bulk Si has an indirect bandgap, whereas SiNWs behave like direct bandgap materials due to the quantum confinement in nano, improving its optoelectronic properties.^{45,46} In addition, chemically etched SiNWs show a higher absorption due to the enhanced rough surface area compared with that of the planar Si surface due

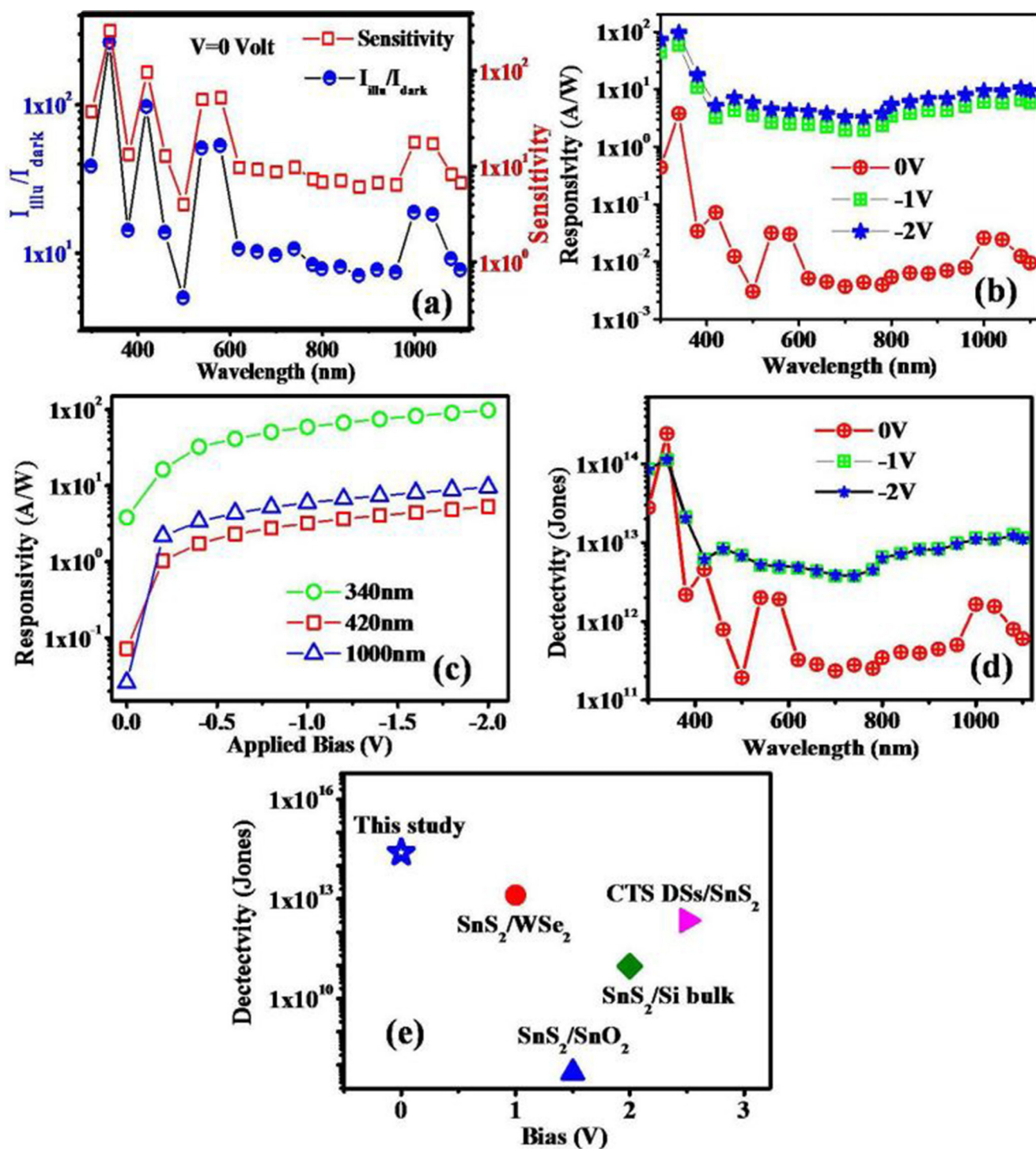


FIG. 6. (a) Dynamic on/off photoresponse and sensitivity of the heterostructure excited by 340 nm light at a 0 volt applied bias. (b) The calculated photoresponsivity of the device plotted as a function of the wavelength of incident light. (c) Photoresponsivity as a function of applied bias approaching saturation at a higher bias. (d) Detectivity of the device at a different bias plotted as a function of the wavelength of incident light. (e) The SnS₂/SiNW heterostructure shows the highest detectivity compared with the other reported SnS₂ based heterostructure devices.

TABLE I. Comparison of the performance parameters of different SnS₂ based photo detectors.

Material and devices	Responsivity	Detectivity (Jones)	Wavelength range (nm)	Opt. power density	Working voltage (V)	References
SnS ₂ NP/SiNW	10 ² A/W >3 A/W	1.14 × 10 ¹⁴ >3.85 × 10 ¹²	340 400–1100	0.54 nW/cm ²	2	This work
SnS ₂ /Si	0.12 A/W	9.35 × 10 ¹⁰	405–808	0.5 mW/cm ²	2	18
CTS QDs/SnS ₂ nanosheet	1 A/W >0.1 A/W	2.25 × 10 ¹² >0.25 × 10 ¹¹	320 400–1100	23.74 μW/cm ²	2.5	19
SnS ₂ /WSe ₂	244 A/W	1.29 × 10 ¹³	550	3.77 mW/cm ²	1	40
SnS ₂ /SnO ₂	2.9 mA/W	5.9 × 10 ⁷	365		1.5	17
SnS ₂ nanoflakes	0.64 μA/W >5.5 nA/W	365 650–850	5.35 μW	5	41
SnS ₂ /hBN TFT	0.6 mA/W	5 × 10 ⁶	300–1000	23.5 μW/cm ²	0.1	42

to multiple reflections.⁴⁷ These are the reasons why SiNW/SnS₂ exhibits much improved results than that based on bulk Si. A comparative study of our SnS₂/SiNW device which shows high responsivity and ultrahigh detectivity with some state-of-the-art photodetectors based on SnS₂ is given in Table I. This comparative study clearly reveals the excellent optoelectronic performance of our reported device with minimum power consumption.

D. Switching characteristics

The time-dependent photocurrent of the SnS₂/SiNW photodetector was investigated under self-bias as well as with a bias dependent condition and is displayed in Fig. 7(a). The rise/fall time is usually defined as the amount of time required for the

photocurrent to measure the growth and decay of the signals from 10% to 90%/90% to 10%, respectively. Due to the unavailability of high precision instruments like oscilloscope or chopper, illumination on the sample was turned on and off manually to measure the response speed of the detector and is presented in Figs. 7(a) and 7(b) at zero bias. This gives a rough estimate but not the actual response speed of the detector.

The rise and fall times for the manual on/off of the illuminated source were 0.9 s and 0.6 s, respectively, for this device, which even yielded a very good performance compared with a few SnS₂ or SnO₂ chalcogenide based photodetectors reported earlier.^{48–50} The actual response speed would be smaller than what we have measured manually. The rise/fall times were reduced to 0.4 s/0.4 s, respectively, when an external bias of –2 V was applied, as shown

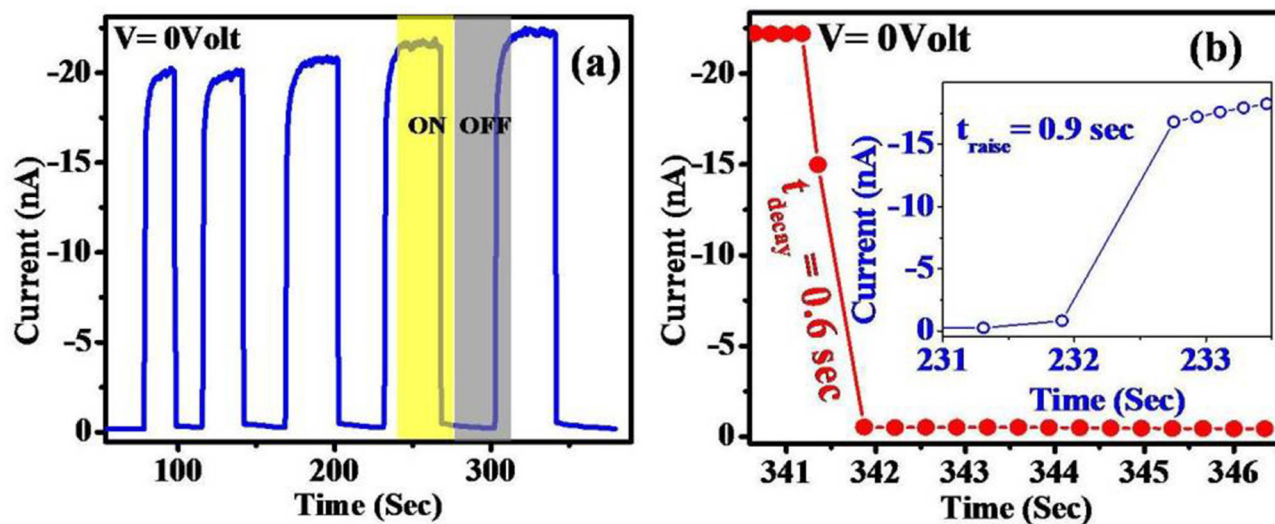


FIG. 7. (a) Dynamic on/off photoresponse of the heterostructure excited by a broadband solar simulator (AM 1.5, 100 mW/m²) light at a 0 V biased voltage. (b) Zoom-in views of the time-resolved photoresponse at V = 0 Volt, identifying the typical rise (inset) and decay time. (c) Dynamic on/off photoresponse of the heterostructure excited with the same broadband solar simulator light at a –2 V biased voltage. (d) Zoom-in views of the time-resolved photoresponse at V = –2 V, identifying the typical rise and fall time (inset).

in Figs. 7(c) and 7(d). This reduction in the rise/fall times may be due to the enhanced collection efficiency of photogenerated carriers under biased conditions. Although the dark current is increased with increasing the bias voltage, and this variation cannot be ignored, the enhanced photoelectric response speed of the device is due to the applied bias voltages. More significantly, after several measurement cycles, the switching of the photocurrent still remains identical, confirming that the as-fabricated device can be used as a self-driven photodetector with little on-chip power consumption. Additionally, the photodetector can maintain a very low dark current of $\sim 5 \times 10^{-10}$ A, and a high on/off ratio of $\sim 3 \times 10^2$ is at the self-power mode, as shown in Fig. 6(a). These characteristics would be favorable for low noise and highly sensitive photodetectors. Furthermore, the measurement result reveals that the photocurrent switching performance of the device can be modulated by the applied reverse bias voltages. As shown in Fig. 7(c), the amplitude of the photocurrent switching of the detector strongly depends on the applied external bias voltage, and the photocurrent monotonically increases from ~ 22 nA at self-bias to ~ 76 μ A as the reverse bias voltage increases to -2.0 V. Additionally, the external applied bias also assists to aid the potential height of the heterostructure [Fig. 5(f)], which increase the separation efficiency of the photogenerated carriers and effectively reduce the recombination rate of the electron-hole pairs. Therefore, applied external biases can influence the photocurrent, responsivity, and detectivity of heterostructure devices.

IV. CONCLUSIONS

In summary, we have fabricated a vertically aligned SiNW/SnS₂ heterostructure with an easy and cost-effective synthesis process. The fabricated heterostructure photodetector shows excellent optoelectronic properties in the UV-Vis-NIR range (300–1100 nm) due to the strong light absorption for these bands by synthesized nanostructures and their high surface-to-volume ratio. The optical sensitivity of the photodetector is found to be as high as $\sim 10^2$ for a 340 nm wavelength and $>10^1$ for the UV to NIR region at a 0 V applied bias with a significantly small optical power (~ 53.75 nW/mm²). The on/off ratio is $\sim 10^2$ at the self-bias condition and response speed is below one second, which is better than those of the few reported chalcogenide based photodetectors. The heterostructure device exhibited a responsivity of ~ 3.8 A/W at self-bias and $\sim 10^2$ A/W at a -2 V applied bias, which are the highest in Si/SnS₂ based heterostructures reported to date. The measured detectivity is as high as $\sim 10^{14}$ Jones at a 340 nm wavelength and $\geq 3.85 \times 10^{12}$ Jones at the 400–1100 nm wavelength range. The observed detectivity of the device is better than that of many similar types of reported detectors, which makes this detector very suitable for a noisy environment. The fabricated device can be used in a broad range of applications and in devices such as low-cost high sensitivity broadband photodetectors.

SUPPLEMENTARY MATERIAL

See the [supplementary material](#) for the growth mechanism of Si nanowires by the MACE method and SnS₂/SiNW stepwise device fabrication process.

ACKNOWLEDGMENTS

Financial support from the Department of Science and Technology, Government of India (Grant No. IFA 15-MS-70) is gratefully acknowledged. R. Basori specially thanks Professor S. K. Ray for allowing the use of the I-V measurement setup. R. Basori also acknowledges the Central Research Facility, IIT Kharagpur, for providing the authors with the structural characterization tools.

REFERENCES

- 1H. Arora, R. Dong, T. Venanzi, J. Zscharschuch, H. Schneider, M. Helm, X. Feng, E. Cánovas, and A. Erbe, "Broadband photodetectors: Demonstration of a broadband photodetector based on a two-dimensional metal-organic framework," *Adv. Mater.* **32**(9), 2070071 (2020).
- 2J. Cheng, X. Huang, D. Wu, Y. Tian, J. Guo, Z. Zhao, Z. Shi, Y. Tian, J. Jie, and X. Li, "Ultrasensitive self-driven broadband photodetector based on 2D-WSe₂/GaAs type-II zenerheterojunction," *Nanoscale* **12**, 4435–4444 (2020).
- 3J. Xu, C. Li, H. Si, X. Zhao, L. Wang, S. Jiang, D. Wei, J. Yu, X. Xiu, and C. Zhang, "3D SERS substrate based on Au-Ag bi-metal nanoparticles/MoS₂ hybrid with pyramid structure," *Optics Express* **26**(17), 21546–21557 (2018).
- 4C. Zhang, C. Li, J. Yu, S. Jiang, S. Xu, C. Yang, Y. J. Liu, X. Gao, A. Liu, and B. Man, "SERS activated platform with three-dimensional hot spots and tunable nanometer gap," *Sens. Actuators B* **258**, 163–171 (2018).
- 5H. Wang and D. H. Kim, "Perovskite-based photodetectors: Materials and devices," *Chem. Soc. Rev.* **46**(17), 5204–5236 (2017).
- 6H. Figgemeier, M. Benecke, K. Hofmann, R. Oelmaier, A. Sieck, J. Wendler, and J. Ziegler, "SWIR detectors for night vision at AIM," in *Infrared Technology and Applications XL* (SPIE, 2014), Vol. 9070, p. 907008.
- 7S. M. Sze and K. K. Ng, *Physical Semiconductor Devices* (Wiley, Hoboken, NJ, 2006).
- 8G. Wang, Y. Zhang, C. You, B. Liu, Y. Yang, H. Li, A. Cui, D. Liu, and H. Yan, "Two dimensional materials based photodetectors," *Infrared Phys. Technol.* **88**, 149–173 (2018).
- 9Z. Liu, T. Luo, B. Liang, G. Chen, G. Yu, X. Xie, D. Chen, and G. Shen, "High-detectivity InAs nanowire photodetectors with spectral response from ultraviolet to near-infrared," *Nano Res.* **6**(11), 775–783 (2013).
- 10R. B. Jacobs-Gedrim, M. Shanmugam, N. Jain, C. A. Durcan, M. T. Murphy, T. M. Murray, R. J. Matyi, R. L. Moore, and B. Yu, "Extraordinary photo-response in two-dimensional In₂Se₃ nanosheets," *ACS Nano* **8**(1), 514–521 (2014).
- 11S. J. Gibson, B. Kasteren, B. Tekcan, Y. Cui, D. Dam, J. E. M. Haverkort, E. P. A. M. Bakkers, and M. E. Reimer, "Tapered InP nanowire arrays for efficient broadband high-speed single-photon detection," *Nat. Nanotechnol.* **14**(5), 473–479 (2019).
- 12K. Thakar and S. Lodha, "Optoelectronic and photonic devices based on transition metal dichalcogenides," *Mater. Res. Express* **7**(1), 014002 (2020).
- 13Y. Wang, E. Sahadeo, G. Rubloff, C.-F. Lin, and S. B. Lee, "High-capacity lithium sulfur battery and beyond: A review of metal anode protection layers and perspective of solid-state electrolytes," *J. Mater. Sci.* **54**(5), 3671–3693 (2019).
- 14B. Ozdemir and V. Barone, "Thickness dependence of solar cell efficiency in transition metal dichalcogenides MX₂ (M: Mo, W; X: S, Se, Te)," *Sol. Energy Mater. Sol. Cells* **212**, 110557 (2020).
- 15W. Choi, I. Akhtar, D. Kang, Y.-J. Lee, J. Jung, Y. H. Kim, C.-H. Lee, D. J. Hwang, and Y. Seo, "Optoelectronics of multi-junction heterostructures of transition metal dichalcogenides," *Nano Lett.* **20**, 1934–1943 (2020).
- 16H. Choi, J. Lee, S. Shin, J. Lee, S. Lee, H. Park, S. Kwon, N. Lee, M. Bang, and S. B. Lee, "Fabrication of high crystalline SnS and SnS₂ thin films, and their switching device characteristics," *Nanotechnology* **29**, 215201 (2018).
- 17S. Abbas, D.-K. Ban, and J. Kim, "Functional interlayer of In₂O₃ for transparent SnO₂/SnS₂ heterojunction photodetector," *Sens. Actuators A* **293**, 215–221 (2019).

- ¹⁸J. Xu, H. Zhang, Z. Song, Y. Xu, Q. Peng, X. Xiu, Z. Li, C. Li, M. Liu, and B. Man, "SnS₂/Si vertical heterostructure for high-performance photodetection with large photocurrent and fast speed," *Appl. Surf. Sci.* **506**, 144671 (2020).
- ¹⁹S. Mani Yadav and A. Pandey, "Hybrid 2D–0D SnS₂ nanoflakes/CTS QDs-based broadband (UV-visible-NIR) photodetector," *IEEE Trans. Electron Devices* **67**(5), 2008–2015 (2020).
- ²⁰A. J. Lu, R. Q. Zhang, and S. T. Lee, "Stress-induced band gap tuning in ⟨112⟩ silicon nanowires," *Appl. Phys. Lett.* **91**, 263107 (2007).
- ²¹F. Toor, J. B. Miller, L. M. Davidson, W. Duan, M. P. Jura, J. Yim, J. Forziati, and M. R. Black, "Metal assisted catalyzed etched (MACE) black Si optics and device physics," *Nanoscale* **8** (34), 15448–15466 (2016).
- ²²C.-Y. Chen, T. C. Wei, C. T. Lin, and J. Y. Li, "Enhancing formation rate of highly-oriented silicon nanowire arrays with the assistance of back substrates," *Sci. Rep.* **7**(1), 1–7 (2017).
- ²³A. M. Morales and C. M. Lieber, "A laser ablation method for the synthesis of crystalline semiconductor nanowires," *Science* **279**(5348), 208–211 (1998).
- ²⁴S. H. Chaki, M. P. Deshpande, D. P. Trivedi, J. P. Tailor, M. D. Chaudhary, and K. Mahato, "Wet chemical synthesis and characterization of SnS₂ nanoparticles," *Appl. Nanosci.* **3**(3), 189–195 (2013).
- ²⁵L. A. Burton, D. Colombara, R. D. Abellon, F. C. Grozema, L. M. Peter, T. J. Savenije, G. Dennler, and A. Walsh, "Synthesis, characterization, and electronic structure of single-crystal SnS, Sn₂S₃, and SnS₂," *Chem. Mater.* **25**, 4908–4916 (2013).
- ²⁶A. Sanchez-Juarez and A. Ortiz, "Effects of precursor concentration on the optical and electrical properties of Sn_xS_y thin films prepared by plasma-enhanced chemical vapour deposition," *Semicond. Sci. Technol.* **17**(9), 931 (2002).
- ²⁷F. Xiao, P. Ilanchezhian, G. Kumar, H. D. Cho, L. Zhang, A. S. Chan, D. J. Lee, G. N. Panin, and T. W. Kang, "Tunable UV-visible absorption of SnS₂ layered quantum dots produced by liquid phase exfoliation," *Nanoscale* **9**(5), 1820–1826 (2017).
- ²⁸Y. Gonglan, Y. Gong, S. Lei, Y. He, B. Li, X. Zhang, Z. Jin *et al.*, "Synthesis of large-scale atomic-layer SnS₂ through chemical vapor deposition," *Nano Res.* **10**(7), 2386–2394 (2017).
- ²⁹S. H. Chaki, M. P. Deshpande, D. P. Trivedi, J. P. Tailor, M. D. Chaudhary, and K. Mahato, "Wet chemical synthesis and characterization of SnS₂ nanoparticles," *Appl. Nanosci.* **3**(3), 189–195 (2013).
- ³⁰D. Ma, H. Zhou, J. Zhang, and Y. Qian, "Controlled synthesis and possible formation mechanism of leaf-shaped SnS₂ nanocrystals," *Mater. Chem. Phys.* **111**, 391–395 (2008).
- ³¹J. Tauc, "Optical properties and electronic structure of amorphous Ge and Si," *Mater. Res. Bull.* **3**(1), 37–46 (1968).
- ³²F. Toor, J. B. Miller, L. M. Davidson, W. Duan, M. P. Jura, J. Yim, J. Forziati, and M. R. Black, "Metal assisted catalyzed etched (MACE) black Si: Optics and device physics," *Nanoscale* **8** (34), 15448–15466 (2016).
- ³³M. Hasan, M. F. Huq, and Z. H. Mahmood, "A review on electronic and optical properties of silicon nanowire and its different growth techniques," *SpringerPlus* **2**(1), 1–9 (2013).
- ³⁴W. Zhao, Z. Wei, L. Ma, J. Liang, and X. Zhang, "Ag₂S quantum dots based on flower-like SnS₂ as matrix and enhanced photocatalytic degradation," *Materials* **12**(40), 582 (2019).
- ³⁵N. G. Deshpande, A. A. Sagade, Y. G. Gudage, C. D. Lokhande, and R. Sharma, "Growth and characterization of tin disulfide (SnS₂) thin film deposited by successive ionic layer adsorption and reaction (SILAR) technique," *J. Alloys Compd.* **436**(1–2), 421–426 (2007).
- ³⁶L. A. Osminkina, V. A. Sivakov, G. A. Mysov, V. A. Georgobiani, U. A. Natashina, F. Talkenberg, V. V. Solov'yev, A. A. Kudryavtsev, and V. Y. Timoshenko, "Nanoparticles prepared from porous silicon nanowires for bio-imaging and sonodynamic therapy," *Nanoscale Res. Lett.* **9**(1), 1–7 (2014).
- ³⁷G. Guangyang, G. Dai, C. Qian, Y. Liu, Y. Fu, Z. Tian, Y. He *et al.*, "High-performance ultraviolet photodetectors based on CdS/CdS: SnS₂ superlattice nanowires," *Nanoscale* **8**(30), 14580–14586 (2016).
- ³⁸C. Yim, M. O'Brien, N. McEvoy, S. Riazimehr, H. Schäfer-Eberwein, A. Bablich, R. Pawar *et al.*, "Heterojunction hybrid devices from vapor phase grown MoS₂," *Sci. Rep.* **4**, 5458 (2015).
- ³⁹B. Wang, H. Yu, X. Quan, and S. Chen, "Ultra-thin g-C₃N₄ nanosheets wrapped silicon nanowire array for improved chemical stability and enhanced photoresponse," *Mater. Res. Bull.* **59**, 179–184 (2014).
- ⁴⁰R. Basori, K. Das, P. Kumar, K. S. Narayan, and A. K. Raychaudhuri, "Single CuTCNQ charge transfer complex nanowire as ultra high responsivity photodetector," *Opt. Express* **22**(5), 4944–4952 (2014).
- ⁴¹X. Zhou, X. Hu, S. Zhou, H. Song, Q. Zhang, L. Pi, L. Li, H. Li, J. Lü, and T. Zhai, "Tunneling diode based on WSe₂/SnS₂ heterostructure incorporating high detectivity and responsivity," *Adv. Mater.* **30**, 1703286 (2018).
- ⁴²Y. Tao, X. Wu, W. Wang, and J. Wang, "Flexible photodetector from ultraviolet to near infrared based on a SnS₂ nanosheet microsphere film," *J. Mater. Chem. C* **3**(6), 1347–1353 (2015).
- ⁴³D. Chu, S. W. Pak, and E. K. Kim, "Locally gated SnS₂/hBN thin film transistors with a broadband photoresponse," *Sci. Rep.* **8**(1), 1–8 (2018).
- ⁴⁴X.-W. Tong, Z.-X. Zhang, D. Wang, L.-B. Luo, C. Xie, and Y.-C. Wu, "Inorganic CsBi₃I₁₀perovskite/silicon heterojunctions for sensitive, self-driven and air-stable NIR photodetectors," *J. Mater. Chem. C* **7**, 863–870 (2019).
- ⁴⁵C. Harris and E. P. O'Reilly, "Nature of the band gap of silicon and germanium nanowires," *Phys. E* **32**(1–2), 341–345 (2006).
- ⁴⁶A. K. Katiyar, A. K. Sinha, S. Manna, and S. K. Ray, "Fabrication of Si/ZnS radial nanowire heterojunction arrays for white light emitting devices on Si substrates," *ACS Appl. Mater. Interfaces* **6**(17), 15007–15014 (2014).
- ⁴⁷K. Das, S. Mukherjee, S. Manna, S. K. Ray, and A. K. Raychaudhuri, "Single Si nanowire (diameter ≤ 100nm) based polarization sensitive near-infrared photodetector with ultra-high responsivity," *Nanoscale* **6**(19), 11232–11239 (2014).
- ⁴⁸W. Tian, T. Zhai, C. Zhang, S.-L. Li, X. Wang, F. Liu, D. Liu *et al.*, "Low-cost fully transparent ultraviolet photodetectors based on electrospun ZnO-SnO₂ heterojunction nanofibers," *Adv. Mater.* **25**(33), 4625–4630 (2013).
- ⁴⁹C. Zhang, Y. Xie, H. Deng, T. Tumlin, C. Zhang, J.-W. Su, P. Yu, and J. Lin, "Monolithic and flexible ZnS/SnO₂ ultraviolet photodetectors with lateral graphene electrodes," *Small* **13**(18), 1604197 (2017).
- ⁵⁰X. Pan, T. Zhang, Q. Lu, W. Wang, and Z. Ye, "High responsivity ultraviolet detector based on novel SnO₂ nanoarrays," *RSC Adv.* **9**(64), 37201–37206 (2019).